



Contents lists available at ScienceDirect

Geochemistry

journal homepage: [www.elsevier.com/locate/chemer](http://www.elsevier.com/locate/chemer)

# Iron isotope constraints on the metal source and depositional environment of the Neoproterozoic banded iron- and manganese deposits in Urucum, Brazil

Qingyu Huang<sup>a</sup>, Sebastian Viehmann<sup>b</sup>, Detlef H.G. Walde<sup>c</sup>, Weiqiang Li<sup>a,\*</sup>

<sup>a</sup> State Key Laboratory for Mineral Deposits Research, School of Earth Sciences and Engineering, Nanjing University, Nanjing, Jiangsu 210023, PR China

<sup>b</sup> Department of Geology, University of Vienna, Althanstrasse 14, 1090 Vienna, Austria

<sup>c</sup> Instituto de Geociências, Universidade de Brasília (UnB), Brasília, Brazil

## ARTICLE INFO

Handling Editor: Carita Augustsson

### Keywords:

Urucum  
Iron formation  
Manganese formation  
Iron isotope  
Bacterial iron reduction  
Neoproterozoic  
Snowball Earth

## ABSTRACT

The Urucum area of Brazil hosts a series of Cryogenian ironstones intercalated by oxide-dominated manganese layers. The Urucum iron and manganese formations (IF-MnF) are among the largest sedimentary iron and associated manganese deposits of the Neoproterozoic, however, the depositional model and the source of metals for the IF-MnF in this area are highly controversial. In this study, we performed systematic Fe isotope analysis on fresh and geochemically characterized drill core samples of the Urucum iron and manganese formation deposited in the center of the ancient Urucum graben system. The samples have a large variation in Fe isotope composition, with a  $\delta^{56}\text{Fe}$  range of  $-2.04\%$  to  $+0.75\%$ , and exhibit a general trend of decreasing  $\delta^{56}\text{Fe}$  values with increasing manganese contents. The low  $\delta^{56}\text{Fe}$  values of the IF and MnF samples reflect Rayleigh fractionation processes of continuous partial oxidation of aqueous Fe(II) prior to deposition at the sampling site. Using a mixing model and previously published Nd isotope data on the same samples, we estimated that benthic (i.e., porewaters released from submarine sediments in the Urucum basin) Fe fluxes provided 7–50% of total Fe in the Urucum IF-MnF, and the rest of Fe source was from low-temperature hydrothermal vents. Based on combined Fe and Nd isotope data of the Urucum IF-MnF, we propose that low-temperature hydrothermal fluids and benthic fluxes of pore waters were mixed and transported by an upwelling current. The fluid subsequently experienced partial oxidation during the transportation process and became enriched in light Fe isotopes. In the Urucum graben basin, the iron- and manganese-rich oxides deposition occurred progressively under increasingly oxidizing conditions, and such process could have operated repeatedly to produce the alternation of iron and manganese formations. The chemical sediments of the Urucum IF-MnF deposits thus reflect the existence of a sharp redox gradient in the marine environment during the late Cryogenian period.

## 1. Introduction

The Neoproterozoic was a critical period in geological history as it witnessed the break-up of the Rodinia supercontinent during the Tonian (e.g., Li et al., 1999), the Snowball (or Slushball) Earth events during the Sturtian (715 to 680 Ma) and Marinoan (650 to 635 Ma) ice ages (e.g., Hoffman et al., 2017; Hyde et al., 2000), and the early radiation of animal life during the Ediacaran (e.g., Erwin et al., 2011). One important geological feature of the Neoproterozoic period was the re-appearance of globally distributed banded iron formations (BIFs). Major events of BIF deposition occurred in the Archean and Paleoproterozoic with a sharp decline of BIF records at 1.8 Ga (Klein, 2005). However, after a

hiatus of about 1 billion years, the widespread occurrence of BIFs resumed in Neoproterozoic successions (Cox et al., 2013; Hoffman et al., 2017). Development of anoxia and accumulation of  $\text{Fe}^{2+}$  in subglacial oceans following the development of Snowball Earth have been invoked to explain the deposition of BIFs during the Neoproterozoic (Kirschvink, 1992; Hoffman et al., 2017). After the Snowball Earth events, the global distribution of banded iron formations disappeared again as a result of more oxygenated and better ventilated oceans. As such, Neoproterozoic iron formations are invaluable archives of the redox and chemical conditions of the Neoproterozoic oceans that set the stage for the biological evolution in the “Ediacaran Garden”.

Among the numerous Neoproterozoic iron formations worldwide,

\* Corresponding author.

E-mail address: [liweiqiang@nju.edu.cn](mailto:liweiqiang@nju.edu.cn) (W. Li).

<https://doi.org/10.1016/j.chemer.2021.125771>

Received 18 December 2020; Received in revised form 24 March 2021; Accepted 10 May 2021

Available online 14 May 2021

0009-2819/© 2021 Elsevier GmbH. All rights reserved.

the iron and manganese formations (IF-MnF) in the Urucum area (Brazil) are of particular importance. First, the high grade and large tonnage of Fe and Mn metals in the Urucum deposits make them economic for mining, which is relatively rare for Neoproterozoic iron formations (Angerer et al., 2020). Second, the majority of the BIFs deposited during the Cryogenian are related to the Sturtian glaciation (Angerer et al., 2020), but the Urucum IF-MnF was likely deposited during the younger Marinoan or even Gaskier ice ages (Viehmann et al., 2016; Hoffman et al., 2011; Piacentini et al., 2013). In other words, the Urucum IF-MnF may represent the end of Neoproterozoic iron formations in the geological record. Third, Mn contents are low (<0.5 wt%) in most banded iron formations and layers of manganese oxides are generally absent in banded iron formations (Klein, 2005), but iron formations are intercalated with four manganese beds in the Urucum deposits (Viehmann et al., 2016; Klein and Ladeira, 2004; Urban et al., 1992; Walde and Hagemann, 2007). Because  $Mn^{2+}$  has a higher redox potential than  $Fe^{2+}$ , deposition of Mn oxides generally occurs at the final stage of a depositional sequence of iron formations under more oxygenated conditions of the ambient atmosphere and hydrosphere systems (Tsikos et al., 2010). Therefore, geochemical signatures in the Urucum IF-MnF records may be used to delineate the waning stages of

Neoproterozoic iron formations deposition and track the transition to atmospheric oxygen levels comparable to the modern-day.

The Urucum IF-MnF deposits have been subjected to extensive studies targeting syn- and post-depositional genetic aspects, however, there are considerable controversies on several aspects of this deposit such as the Fe source and depositional model (Angerer et al., 2016; Freitas et al., 2011; Urban et al., 1992; Viehmann et al., 2016; Angerer et al., 2020); see Walde and Hagemann (2007) for compilation of different ore deposit models. Iron isotopes fractionate significantly between ferric and ferrous phases (e.g., Johnson et al., 2008a, 2008b), and have been demonstrated to be a powerful tool to trace the source of Fe and the processes of Fe cycling in studies of banded iron formations (e.g., Dauphas et al., 2017; Johnson et al., 2008a, 2008b). In this study, we performed systematic Fe isotope analysis for a set of geochemically well-characterized drillcore samples from the Urucum IF-MnF deposit from Viehmann et al. (2016) that were deposited in the center of the ancient Urucum graben system. The Fe isotope data provide new insights into the formation of the Urucum IF-MnF deposits and allow us to better determine their sources in the Late Neoproterozoic Urucum basin.

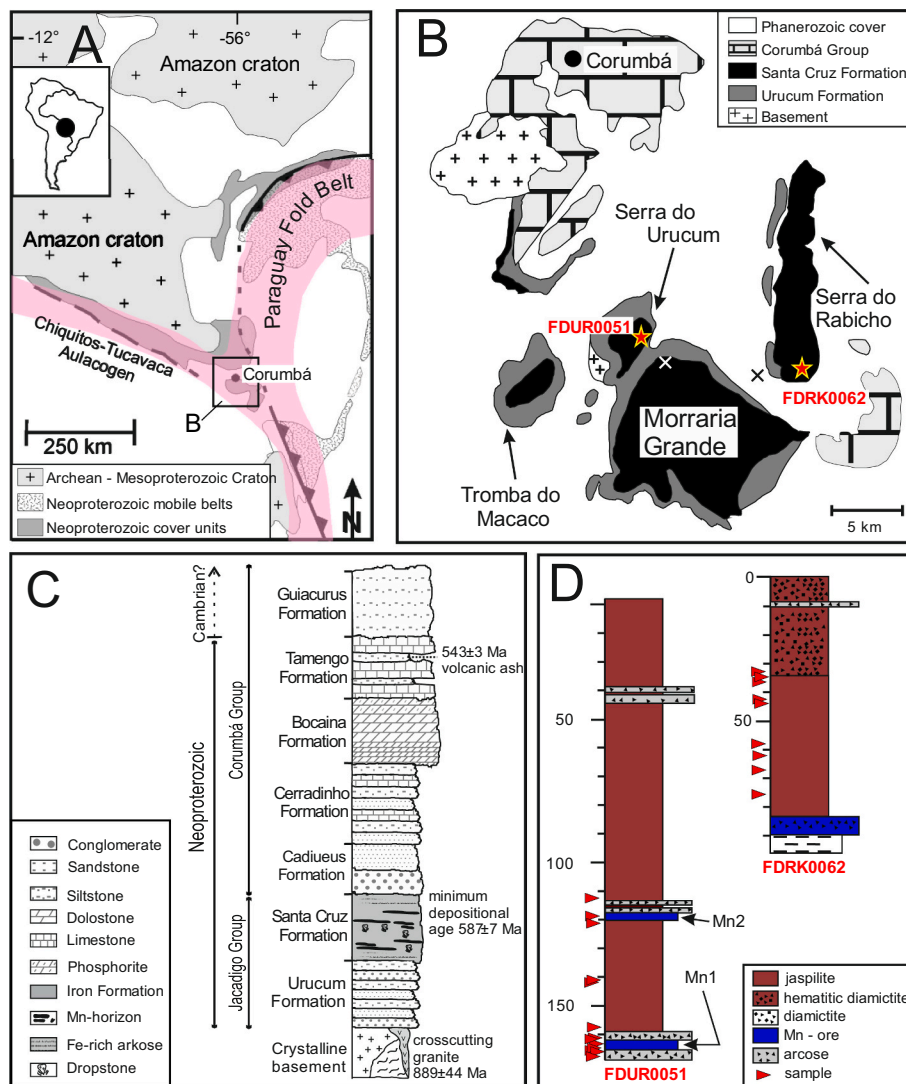


**Fig. 1.** A. Geotectonic setting of the Urucum deposits, with pink shade showing Brasiliano Paraguay fold belt and the Chiquitos-Tucavaca aulacogen; B. a more detailed map of the geology of the Urucum area; C. Stratigraphy of the Urucum area; D. lithocolumn of the two drill cores that were analyzed in this study for Fe isotopes. (For interpretation of the references to color in this figure legend, the reader is referred to the web version of this article.) Modified after Viehmann et al. (2016).

## 2. Geological background and samples

Neoproterozoic iron- and manganese oxide deposits occur in the Urucum district, western Brazil (57°40'W, 19°20'S), near the border between Brazil and Bolivia. The Urucum district is located within the NW-SE trending Chiquitos–Tucavaca aulacogen, surrounded by the Archaean to Mesoproterozoic Amazon Craton to the northwest, the Paleo- to Mesoproterozoic Rio Apa Block to the east, and the Neoproterozoic Paraguay Block to the east (Fig. 1A). The Precambrian crystalline basement of the Urucum district is composed of metamorphosed gneisses that are cross-cut by pegmatitic granite and younger mafic dykes (Urban et al., 1992). U–Pb zircon dating of the basement granites and granitic dropstones within the IF yielded ages of  $1826 \pm 4$  Ma and  $1847 \pm 3$  Ma (Viehmann et al., 2016). The crystalline basement is unconformably overlain by Neoproterozoic sedimentary successions, which can be separated into two groups: (I) the lower Jacadigo Group (comprising the Urucum and Santa Cruz Formations) and (II) the upper Corumbá Group (Fig. 1C).

The siliciclastic Urucum Formation is composed of gray-green, fine to medium-coarse grained siliciclastic rocks with calcitic cement. The transition of the Urucum Formation to the Santa Cruz Formation up section is marked by a change in the cementing mineral, ranging from carbonates in the Urucum Formation to Fe and Mn oxides in the lower Santa Cruz Formation. The lower Santa Cruz Formation (also known as Corrego da Pedras Formation) consists of clastic sediments and granular iron formations with rare glaciomarine dropstones that are intercalated by the first (Mn 1) of four manganese ore horizons. The thickness of Mn1 horizon varies from 0 to 7 m. The upper Santa Cruz Formation (also known as Banda Alta Formation) includes three additional manganese ore horizons (Mn 2 to Mn 4) intercalated in ca. 300 m thick iron formation (hematitic jaspilites). The third and fourth manganese ore horizons (Mn 3 and Mn 4) occur within the hematite-jaspilite succession (e.g., Freitas et al., 2011; Urban et al., 1992).

The stratigraphically overlying Corumbá Group contains Ediacaran index fossils such as *Corumbella weneri* (cf. Walde et al., 2015) and comprises of, from older to younger, the Cadiueu Formation, the Ceradinho Formation, the Bocaina Formation, the Tamengo Formation, and the Guaiacurus Formation (Fig. 1C). U–Pb dating of zircon from a volcanic ash layer within the Tamengo Formation yielded an age of  $543 \pm 3$  Ma (cf. Walde et al., 2015); more recent age determinations via CA-ID-TIMS yield 541.85 to 542.37 Ma for tuff layers in the Tamenga Formation (Parry et al., 2017). The age constraints of the Jacadigo Group, however, are relatively poor. The  $^{40}\text{Ar}/^{39}\text{Ar}$  ages for Mn-bearing minerals cryptomelane (diagenetic age) and braunite (re-crystallization age) are  $587 \pm 7$  Ma and  $547 \pm 3$  Ma, respectively (Piacentini et al., 2013). These dates define the minimum depositional age of the iron formations at Urucum.

The samples analyzed in this study were collected from two drill cores that drilled through the fresh rocks of the Santa Cruz Formation and encounter IF-MnF rocks from the center of the ancient Urucum graben system (Fig. 1B & D) that were not subject to supergene alteration. Notably, unweathered rocks of the Santa Cruz Formation are extremely rare in outcrops due to the intense and deep-reaching laterization in the Urucum district. Drill core FDUR0051 is located in the Serra do Urucum (Fig. 1B) and encounters Mn ore horizons Mn1 and Mn2, jaspilites, and arkoses (Fig. 1D). Drill core FDRK0062 is located in the eastern Serra do Rabicho and encounters hematitic and manganese-rich arkoses, diamictites, arkoses, siltstones, and jaspilites (Fig. 1D). The drill core samples were cut to separate individual Si-, Fe-, and Mn-rich IF/MnF mesobands or clastic layers to avoid contamination of different lithologies such as microbanded detrital intercalations. The positions of samples along the drill core are marked in Fig. 1D; sample pictures and drill core logs with individual sample descriptions are given in the supplement of Viehmann et al. (2016). Individual macroscopic layers of IF and MnF drill cores were cut by a diamond saw and pulverized to fine powders in an agate mill. Subsequently, the

homogeneous powders were analyzed for major and trace elements as well as radiogenic Nd isotopes (Viehmann et al., 2016).

Based on the geochemical characteristics of major and trace elements, samples of the Neoproterozoic Urucum iron formation can be divided into 3 main groups (Fig. 2): 1) iron formation samples with high hematite content that are almost free of detrital contamination (pure IF), 2) iron formation samples that contain detrital (aluminosiliciclastic) components (impure IF), and 3) manganese ore samples that contain more manganese than iron (MnF,  $\pm$ detrital contamination). Pure IF samples have very low contents of  $\text{Al}_2\text{O}_3$ , Ti, and Th, which are below 0.2 wt%, 220 ppm, and 1 ppm, respectively. The impure IF samples and manganese ores samples have much higher and variable contents of  $\text{Al}_2\text{O}_3$  (0.1–8.2 wt%), Ti (50–1700 ppm), and Th (0.5–7 ppm). The impure IF samples and manganese ores samples have overlapping  $\text{Al}_2\text{O}_3$ , Ti, and Th contents, however, they are distinct in Fe/Mn ratio, that the impure IF samples have Fe/Mn ratio below 5 and the Fe/Mn ratios of manganese ores are mostly below 1 (Fig. 2C). Representative sample powders of both drill cores covering IF with the intercalated Mn1 and Mn2 beds were measured for Fe isotopes in this study.

## 3. Analytical methods

Iron isotope measurements were undertaken at the State Key Laboratory for Mineral Deposit Research, Nanjing University. All chemical procedures were performed in a clean room with HEPA filtered air; all apparatus, beakers, centrifuge tubes, and pipette tips were acid-washed before usage; double-distilled acids and deionized ( $>18.2$  M $\Omega$ ) water were used for experiments. Approximately 5 mg of homogeneous rock powder of each sample was weighed and digested in a mixture of 2 mL conc. HCl acid and 2 mL conc.  $\text{HNO}_3$  acid in a Teflon beaker. The beaker was subsequently capped tightly and placed on a hotplate at 130 °C for over 24 h. Then the beaker was uncapped and evaporated at 96 °C on a hotplate. After drying of the solution, 2 mL conc. HCl was added to the beaker and the dissolved samples were heated to dryness again; this procedure was repeated twice to convert the metals to chlorides. After that, 1.1 mL 7 N HCl was added to the beaker to dissolve the sample, and a 0.1 mL aliquot of the dissolved solution was taken and diluted for Fe concentration measurement by ICP-OES. Based on the measured Fe concentration, an aliquot of the dissolved sample solution that contained about 100  $\mu\text{g}$  of Fe was transferred to a new Teflon beaker, dried, and re-dissolved in 0.1 mL 7 N HCl before Fe purification.

Purification of Fe was performed by ion-exchange chromatography using 0.2 mL Bio-Rad AG MP-1 resin that was loaded in a custom-made shrinkable Teflon column (4 mm ID, 26 mm height). Before usage, the resin was pre-cleaned by 1 mL 2% (volume ratio)  $\text{HNO}_3$  and 1 mL deionized  $\text{H}_2\text{O}$  ( $>18.2$  M $\Omega$ ), then conditioned with 2 mL 7 M HCl. After loading 0.1 mL sample solution in 7 M HCl onto the resin, the matrix elements were eluted off the column using 3 mL of 7 M HCl in 0.5 mL increments. Iron was subsequently eluted from the resin using 3 mL of 2%  $\text{HNO}_3$ . The Fe cut was evaporated to dryness, re-dissolved in 100  $\mu\text{L}$  sample in 7 M HCl, and was purified for a second time by repeating the anion exchange procedure as described above. The purified Fe was then dried and treated with three drops of 30%  $\text{H}_2\text{O}_2$  and 2 mL concentrated  $\text{HNO}_3$  to decompose any potential organic matters that were eluted off from the resin. Finally, the purified Fe was dissolved in 4 mL 2%  $\text{HNO}_3$  for mass spectrometry analysis. Recovery of Fe for the ion exchange procedure was monitored for each sample by measuring the Fe contents in the purified Fe cut and the matrix element cuts using ICP-OES, and the Fe recovery was always  $>95\%$ .

Iron isotope ratios were measured on a Neptune Plus MC-ICP-MS at Nanjing University. The instrument was running at “wet-plasma”, high-mass resolution mode, using a 100  $\mu\text{L}/\text{min}$  self-aspirating nebulizer tip and a glass spray chamber. Under such a setting, the instrument sensitivity was 4–6 V/ppm on  $^{56}\text{Fe}^+$ . Molecular interferences of  $^{40}\text{Ar}^{14}\text{N}^+$  and  $^{40}\text{Ar}^{16}\text{O}^+$  on  $^{54}\text{Fe}^+$  and  $^{56}\text{Fe}^+$  were fully resolved under the high mass resolution mode (mass resolving power: 7000–1000). Isobaric

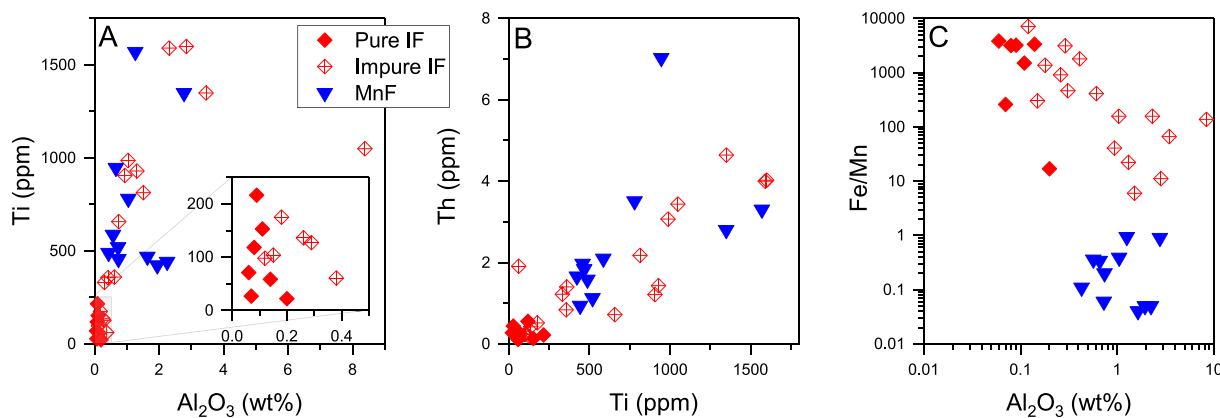


Fig. 2. Cross plots of major and trace elements for the drill core samples from the Urucum IF-MnF deposit. Source data are from Viehmann et al. (2016).

interference of  $^{54}\text{Cr}^+$  on  $^{54}\text{Fe}^+$  was monitored by simultaneous measurement of  $^{53}\text{Cr}^+$  signals and was corrected offline. A standard-sample-standard bracketing routine was applied for the correction of mass bias and instrumental drift. All samples were diluted to  $2 \pm 0.2$  ppm to match the concentration of an in-house standard that was constant at 2.0 ppm. Each isotope analysis consists of a 40 s measurement of on-peak acid blank, and fifty 4-s integrations on the Fe solutions. The internal precision (2 standard error or 2 SE) was typically better than  $\pm 0.03\text{‰}$  for  $^{56}\text{Fe}/^{54}\text{Fe}$  and  $\pm 0.05\text{‰}$  for  $^{57}\text{Fe}/^{54}\text{Fe}$ . The long-term external reproducibility (2 standard deviation or 2SD) of Fe isotope analysis is better than  $\pm 0.08\text{‰}$  in  $^{56}\text{Fe}/^{54}\text{Fe}$  and  $\pm 0.15\text{‰}$  in  $^{57}\text{Fe}/^{54}\text{Fe}$  based on repeat

analysis of multiple Fe isotope standard solutions against in-house stock solutions.

Iron isotope compositions are reported as  $\delta^{56}\text{Fe}$  (in unit of per mil or ‰) relative to the international standard of IRMM-014:

$$\delta^{56}\text{Fe}_{\text{sample}} = \left[ \left( \frac{^{56}\text{Fe}}{^{54}\text{Fe}} \right)_{\text{sample}} / \left( \frac{^{56}\text{Fe}}{^{54}\text{Fe}} \right)_{\text{IRMM-014}} - 1 \right] \times 1000$$

Accuracy of Fe isotope measurements was confirmed by repeated measurements of different Fe solution standards and USGS rock standards that were treated as unknowns with the Urucum IF-MnF samples.  $\delta^{56}\text{Fe}$  of two ultrapure Fe solutions from University of Wisconsin-Madison, J-M Fe and HPS Fe, are  $0.37 \pm 0.06\text{‰}$  ( $n = 10$ , 2SD) and

Table 1

Iron isotope data for drill core samples from Urucum. Sample ID followed Viehmann et al. (2016). n denotes the number of Fe isotope analysis, and 2SD denotes 2 standard deviation of the repeated analysis.

Sample ID	Drill core depth (m)	Type	$\delta^{56}\text{Fe}$	2SD	$\delta^{57}\text{Fe}$	2SD	n
UR51_5	117.95–118.15	Impure IF	-0.27	0.04	-0.38	0.12	3
UR51_10	120.20–120.30	Impure IF	-0.14	0.06	-0.18	0.00	2
UR51_14	120.95–121.00	MnF	-1.83	0.19	-2.67	0.22	2
UR51_15	120.95–121.00	MnF	-1.93	0.06	-2.83	0.01	2
UR51_16	120.95–121.00	MnF	-1.90	0.11	-2.76	0.20	2
UR51_17	121.25–121.35	MnF	-1.70	0.07	-2.51	0.10	3
UR51_20	143.25–143.45	Pure IF	-0.67	0.02	-0.97	0.06	2
UR51_21	143.25–143.45	Impure IF	-2.04	0.07	-3.01	0.10	3
UR51_25	158.25–158.45	Impure IF	-1.87	0.02	-2.72	0.02	2
UR51_30	161.30–161.50	Impure IF	-0.52	0.03	-0.73	0.13	2
UR51_31	161.30–161.50	Impure IF	-0.55	0.04	-0.80	0.07	2
UR51_36	163.15–163.35	Impure IF	-0.66	0.07	-0.98	0.13	2
UR51_40	163.85–164.05	Impure IF	-0.45	0.06	-0.64	0.00	2
UR51_42	163.85–164.05	Impure IF	-0.57	0.07	-0.85	0.17	2
UR51_45	164.55–164.35	MnF	-1.73	0.06	-2.53	0.05	3
UR51_47	164.55–164.35	Impure IF	-1.35	0.13	-1.92	0.11	3
UR51_50	165.00–165.15	MnF	-1.82	0.06	-2.61	0.10	3
UR51_51	165.00–165.15	MnF	-1.84	0.08	-2.71	0.10	2
UR51_52	165.45–165.55	MnF	-1.69	0.06	-2.50	0.06	2
UR51_53	165.45–165.55	MnF	-1.80	0.08	-2.66	0.07	2
UR51_55	166.40–166.50	MnF	-2.00	0.07	-2.96	0.04	3
UR51_56	166.40–166.50	MnF	-1.75	0.08	-2.59	0.09	3
UR51_60	167.25–167.40	Impure IF	0.75	0.15	1.12	0.24	4
UR51_65	168.10–168.25	Impure IF	0.32	0.11	0.49	0.19	4
UR51_70	168.75–168.85	Impure IF	-0.22	0.05	-0.32	0.02	2
UR51_75	169.35–169.50	Impure IF	0.44	0.06	0.67	0.12	4
UR62_10	34.95–35.00	Pure IF	-1.16	0.13	-1.67	0.17	3
UR62_11	34.95–35.00	Impure IF	-0.58	0.07	-0.85	0.15	2
UR62_15	43.70–43.90	Pure IF	-0.84	0.01	-1.24	0.08	3
UR62_16	43.70–43.90	Pure IF	-0.82	0.11	-1.19	0.16	4
UR62_17	43.70–43.90	Pure IF	-0.77	0.02	-1.11	0.03	2
UR62_18	43.70–43.90	Impure IF	-0.92	0.10	-1.38	0.13	2
UR62_25	58.60–58.70	Pure IF	-1.24	0.08	-1.83	0.15	3
UR62_26	58.60–58.70	Pure IF	-1.15	0.06	-1.71	0.06	2
UR62_30	62.25–62.30	Pure IF	-1.68	0.08	-2.44	0.16	5
UR62_31	62.25–62.30	Impure IF	-1.11	0.13	-1.64	0.15	2

$0.58 \pm 0.06\%$  ( $n = 7$ , 2SD), respectively, which are in excellent agreement with the recommended values ( $0.34\%$  for J-M and  $0.58\%$  for HPS, respectively; Beard et al., 2003). In addition, the measured Fe isotope compositions of the international whole-rock standards, DNC-1a ( $\delta^{56}\text{Fe} = 0.02 \pm 0.06\%$ ,  $n = 3$ ), BCR-2 ( $\delta^{56}\text{Fe} = 0.11 \pm 0.08\%$ ,  $n = 9$ ), BHVO-2 ( $\delta^{56}\text{Fe} = 0.13 \pm 0.05\%$ ,  $n = 9$ ), BIR-1a ( $\delta^{56}\text{Fe} = 0.08 \pm 0.06\%$ ,  $n = 3$ ) and DTS-2b ( $\delta^{56}\text{Fe} = 0.06 \pm 0.08\%$ ,  $n = 3$ ), are all consistent with the recommended values in literature ( $0.05 \pm 0.02\%$  for DNC-1,  $0.09 \pm 0.01\%$  for BCR-2,  $0.11 \pm 0.01\%$  for BHVO-2,  $0.05 \pm 0.02\%$  for BIR-1a, and  $0.03 \pm 0.01\%$  for DTS-2b; Craddock and Dauphas, 2011) within analytical uncertainties.

#### 4. Results

The samples analyzed from two drill cores show a large variation in  $\delta^{56}\text{Fe}$  values, from  $-2.04\%$  to  $+0.75\%$  (Table 1).  $\delta^{56}\text{Fe}$  values of pure IF, impure IF, and MnF samples range from  $\delta^{56}\text{Fe} = -1.68\%$  to  $-0.67\%$ ,  $-2.04\%$  to  $0.75\%$ , and  $-2.00\%$  to  $-1.69\%$ , respectively. The high  $\delta^{56}\text{Fe}$  values are measured from impure IF samples in the lower part of drill core FDUR0051 (Fig. 3), other than that, there is no clear stratigraphic trend in  $\delta^{56}\text{Fe}$  along the drill core. However, there is a remarkable correlation between Fe/Mn ratio and  $\delta^{56}\text{Fe}$  value of the samples from both drill cores, and the MnF samples have distinctively low  $\delta^{56}\text{Fe}$  values (Fig. 3).

In a three-isotope space of linearized  $\delta^{56}\text{Fe}'$  versus  $\delta^{57}\text{Fe}'$  (Fig. 4), the data plot along a linear trend with a best-fit slope of  $0.6810 \pm 0.010$  (2SD), which is consistent with the theoretical slope (0.6780) that corresponds to equilibrium Fe isotope fractionation (Young et al., 2002). It should be noted, however, that this slope also marginally overlaps with the theoretical slope (0.6720; i.e., Young et al., 2002) when considering the 2SD uncertainty for data regression. Nonetheless, the slope data for the samples confirms that the Fe isotope analyses were performed without impacts of interference.

#### 5. Discussions

##### 5.1. Fe isotope variability in the Urucum IF and MnF samples

Iron isotope variation in chemical sediments could originate from isotopic heterogeneity of aqueous  $\text{Fe}^{2+}$  (e.g., Li et al., 2015) and isotope fractionation during oxidation of  $\text{Fe}^{2+}$  (e.g., Johnson et al., 2008a, 2008b). Iron in banded iron formations can be sourced from hydrothermal vents that had  $\delta^{56}\text{Fe}$  values of  $-0.5$  to  $0\%$  (e.g., Johnson et al., 2008a, 2008b), or pore fluids from coastal sediments where bacterial iron reduction released  $\text{Fe}^{2+}$  with low  $\delta^{56}\text{Fe}$  values ( $-0.5$  to  $-3.5\%$ ) (Homoky et al., 2009; Severmann et al., 2006). Although the  $\delta^{56}\text{Fe}$  values of the Urucum IF ( $-2.04\%$  to  $0.75\%$ ) and MnF ( $-2.00\%$  to  $-1.69\%$ ) samples are mostly within the range of the two potential Fe

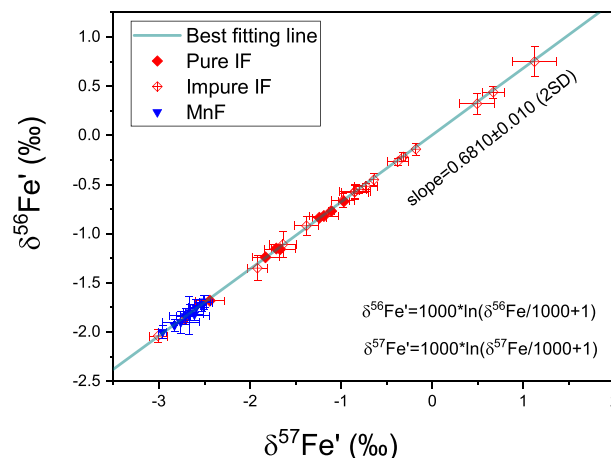


Fig. 4. Three isotope plot of the linearized Fe isotope data for the Urucum IF and MnF samples, the best fitting slope is obtained by the software 'Origin'.

sources, the range of Fe/Mn ratio of potential sources for iron formations is rather limited compared to the range of Fe/Mn ratios of the drill core samples (Fig. 5A). The Fe/Mn ratio of pore fluids in sediments released by bacterial iron reduction varies between 2 and 10 (Haley et al., 2004), which is similar to the Fe/Mn ratio (1 to 12) of hydrothermal fluids at  $350$ – $450$  °C (Pester et al., 2011). Therefore, the Fe isotope variability of the Urucum IF and MnF should not be directly inherited from hydrothermal and biologically recycled Fe sources by complete single-stage  $\text{Fe}^{2+}$  oxidation, because such a mechanism cannot account for the observed variability of high and low Fe/Mn ratio of the precipitates at the same time. This statement is corroborated by the lack of positive, shale-normalized Eu anomalies in the Urucum IF-MnF suggesting that high-temperature ( $>250$  °C), hydrothermal did not affect seawater chemistry in the Urucum basin (Viehmann et al., 2016).

A distinct feature in Fig. 5A is the positive correlation of  $\delta^{56}\text{Fe}$  and Fe/Mn (in log scale) for samples with  $\delta^{56}\text{Fe}$  less than  $-0.2\%$ . Such a trend can also be found in several Archean and Paleoproterozoic banded iron and manganese formations (Fig. 5B) (Tsikos et al., 2010; Kurzweil et al., 2016). The similarity in the trends of data on a plot of  $\delta^{56}\text{Fe}$  versus  $\log(\text{Fe}/\text{Mn})$  for iron and manganese formations of different ages implies that a common process may have governed the variability in both  $\delta^{56}\text{Fe}$  and Fe/Mn ratio in iron formations. During partial oxidation of aqueous  $\text{Fe}^{2+}$ , heavy Fe isotopes preferentially partition into the oxidation product (e.g., Fe(III)-hydroxides), leading to lower  $\delta^{56}\text{Fe}$  values for the remaining aqueous  $\text{Fe}^{2+}$  (e.g., Li et al., 2013). On the other hand, due to the higher redox potential of  $\text{Mn}^{4+}/\text{Mn}^{2+}$  relative to that of  $\text{Fe}^{3+}/\text{Fe}^{2+}$ ,  $\text{Mn}^{2+}$  in aqueous solutions is not oxidized when  $\text{Fe}^{2+}$  already started to

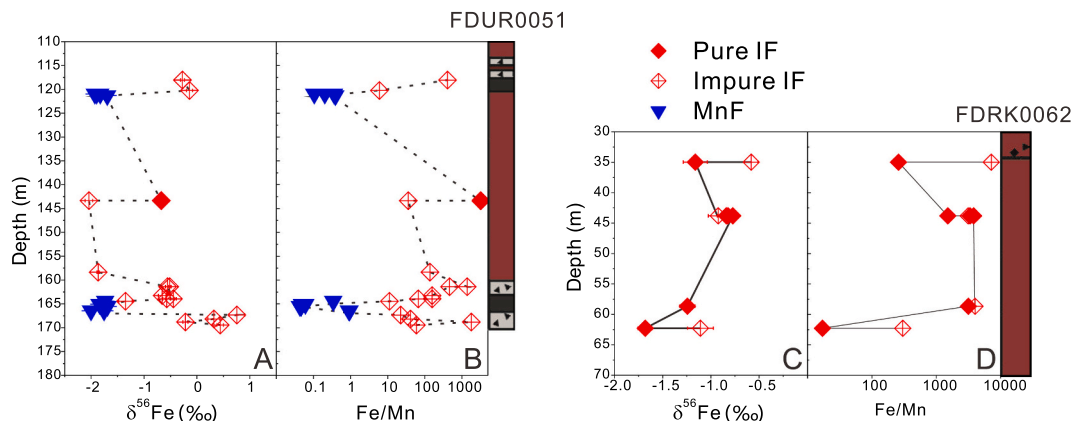
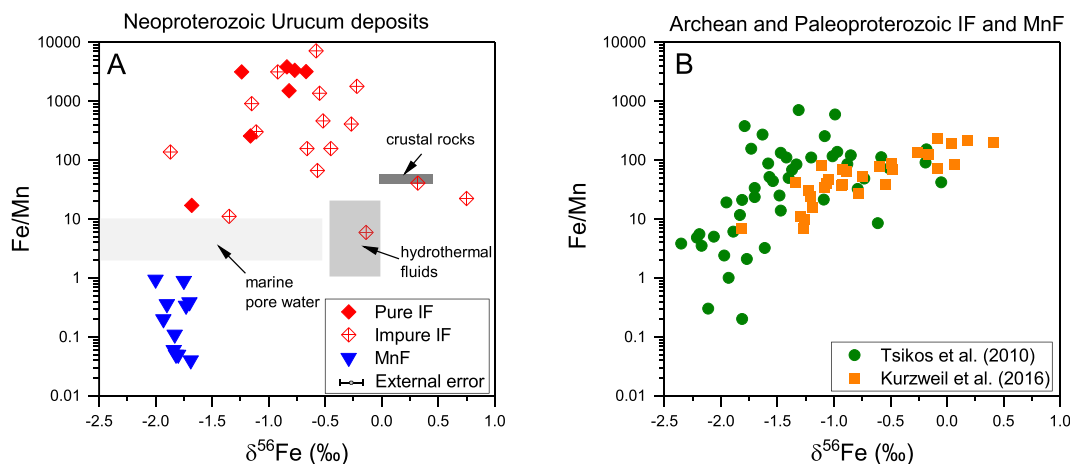


Fig. 3. Variability of  $\delta^{56}\text{Fe}$  and Fe/Mn ratios for different types of samples in the two drill cores from the Urucum deposits.



**Fig. 5.** Cross plots of (A)  $\delta^{56}\text{Fe}$  versus Fe/Mn for the IF and MnF samples from the Neoproterozoic Urucum deposits, and (B) two Archean and Paleoproterozoic iron formations in literature (Tsikos et al., 2010; Kurzweil et al., 2016). The gray shaded rectangles in plot A represent the ranges of Fe/Mn and  $\delta^{56}\text{Fe}$  values of potential iron sources for the Urucum formations (details are given in the discussion).

partially oxidize to Fe(III)-hydroxides and is subsequently removed from the water body. Even if oxidation of  $\text{Mn}^{2+}$  could have occurred above a redoxcline, the oxidation product of aqueous manganese (e.g.,  $\text{MnOOH}$ ) can be readily reduced by  $\text{Fe}^{2+}$  in the water body and soft sediment below the redox-cline following the equation:  $\text{MnOOH} + \text{Fe}^{2+} \rightarrow \text{FeOOH} + \text{Mn}^{2+}$  (Tsikos et al., 2010; Kurzweil et al., 2016). As such, the net reaction is still partial oxidation of  $\text{Fe}^{2+}$  below the redoxcline without oxidative removal of  $\text{Mn}^{2+}$  from the water body. Therefore, partial oxidation under a (semi)closed system conditions would result in the decrease of  $\delta^{56}\text{Fe}$  values and the Fe/Mn ratio in the aqueous solution at the same time, and subsequent partial oxidation of the remaining fluid would magnify the decrease in both  $\delta^{56}\text{Fe}$  and Fe/Mn, following a Rayleigh fractionation process. Accordingly, Fe(III)-hydroxides precipitated from the evolving fluid would show progressively lower  $\delta^{56}\text{Fe}$  and Fe/Mn values (Fig. 5A, B).

A numeric model is employed to quantitatively understand the co-variation in  $\delta^{56}\text{Fe}$  and Fe/Mn values. The model is a Rayleigh-type model similar to that has been described in detail by Nie et al. (2020), which simulates the progressive partial oxidation of a water mass that has an initial  $\delta^{56}\text{Fe}$  value of  $-0.5\text{‰}$  and an initial Fe/Mn ratio of 5. The water mass is assumed to experience progressive partial oxidation, with an apparent Fe isotope fractionation factor of  $\Delta^{56}\text{Fe}$  ( $\Delta^{56}\text{Fe}_{\text{solid-aq}} =$

$\delta^{56}\text{Fe}_{\text{solid}} - \delta^{56}\text{Fe}_{\text{aqueous}}$ ) and a Mn partition coefficient of  $k$  ( $k = (\text{Mn}/\text{Fe})_{\text{solid}}/(\text{Mn}/\text{Fe})_{\text{aqueous}}$ ) between the Fe(III) hydroxide precipitate and the remaining aqueous solution. Selected modeling results for the Fe(III) hydroxide precipitate are plotted in Fig. 5, which shows that a  $\Delta^{56}\text{Fe}$  fractionation factor of 0.5‰ to 1‰ is required to reproduce the general trend (slope) of the majority of the Urucum IF samples. This fractionation factor is remarkably smaller than the equilibrium Fe isotope fractionation factor between Fe(III) hydroxide and aqueous Fe(II) (i.e.,  $\sim 3\text{‰}$ , Johnson et al., 2008a, 2008b), indicating kinetic isotope fractionation occurred during precipitation of the Urucum IF. Further, to cover the majority of the data range of the IF samples by modeling, a range of 0.05 to 0.0005 for Mn partition coefficient  $k$  is needed as the modeling parameter. Such range (two orders of magnitude) of  $k$  is unreasonably large for the adsorption process in seawater; thus, the Mn/Fe ratios of the IF samples were most presumably altered by post-depositional processes such as diagenesis.

The MnF samples plot below the Rayleigh evolution trend defined by the majority of the IF samples (Fig. 6). The MnF samples have  $\delta^{56}\text{Fe}$  values overlapping with Mn-rich (low Fe/Mn) IF samples but at lower Fe/Mn ratios. This is best explained by the dominance of  $\text{Mn}^{2+}$  oxidation over  $\text{Fe}^{2+}$  oxidation in a high redox potential environment, where complete oxidation of aqueous  $\text{Fe}^{2+}$  occurred and Fe isotope

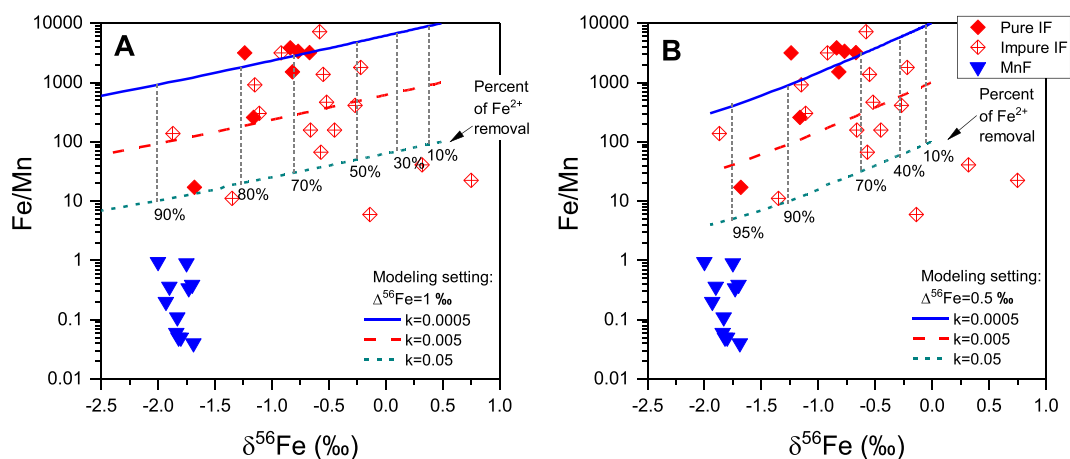


**Fig. 6.** Rayleigh modeling of evolution of the  $\delta^{56}\text{Fe}$  and Fe/Mn ratio of the Fe(III) hydroxide precipitate assuming partial oxidation of a water mass that has an initial  $\delta^{56}\text{Fe}$  of  $-0.5\text{‰}$  and an initial Fe/Mn ratio of 5. Plot A shows the results assuming a  $\Delta^{56}\text{Fe}$  fractionation factor of 1‰ and three different  $k$  factors; Plot B shows the results assuming a  $\Delta^{56}\text{Fe}$  fractionation factor of 0.5‰ and three different  $k$  factors. The colored lines denote the trajectory of the modeling results, and the numbers below the lines mark the degree of Fe(II) removal by partial oxidation at the corresponding  $\delta^{56}\text{Fe}$  values.

fractionation of the water mass stopped. Based on the numeric modeling, it is estimated that  $\text{Mn}^{2+}$  oxidation started to be the dominant process when 90% to 95% of the aqueous Fe(II) was deposited by progressive oxidation. Additionally, there are three IF samples that have intermediate Fe/Mn ratios but high  $\delta^{56}\text{Fe}$  values, plotting outside of the general trend for samples with  $\delta^{56}\text{Fe} < -0.2\text{‰}$  (Fig. 6A). These samples are impure IF samples from the strata below the first manganese ore horizon (Mn1; Figs. 1, 3). As this strata contains dropstones and glacial debris (Walde and Hagemann, 2007; Urban et al., 1992), the anomalous  $\delta^{56}\text{Fe}$ -Fe/Mn signatures of the three samples could be caused by mixing of materials with high  $\delta^{56}\text{Fe}$  values such as high-Si igneous rocks (Walde and Hagemann, 2007; Urban et al., 1992) or Fe(III)-hydroxide precipitates by early-stage partial oxidation of aqueous Fe(II).

## 5.2. Quantifying the contributions of different iron sources to the Urucum IF and MnF

The metal source of Fe and Mn for the ancient Urucum depositional system is controversial. Urban et al. (1992) hypothesized that Fe and Mn were released from (bacterial) reduction of metal oxides in glacial deposits in the lower Jacadigo Group. By contrast, Freitas et al. (2011) argued that the metals in the Urucum deposits were sourced from hydrothermal activities related to regional faulting and rifting. Angerer et al. (2016) suggested that metal sources of hydrothermal and pore-water origins both contributed to the Urucum deposits, but gave no discussion on the relative contributions of the two sources. Viehmann et al. (2016) performed a systematic Nd isotope study on fresh drill core samples from the Urucum deposits, and reported significant variations in  $\epsilon\text{Nd}_t$  between basement rocks, IF and MnF samples, dropstones, and clastic sediments. The samples in Viehmann et al. (2016) were analyzed for Fe isotopes in this study and a combination of the elemental and isotopic ratios of Fe and Nd is employed here to constrain the contributions of different iron sources to the Neoproterozoic Urucum environment.

The crystalline basement rock of the Rio Apa block and dropstone samples in the Urucum region have initial  $\epsilon\text{Nd}_t$  values of about  $-14$ , whereas the clastic components of the Urucum successions have  $\epsilon\text{Nd}_t$  values of about  $-8$ , similar to detrital components of the Amazonia Craton, suggesting that dropstones and clastic sediments in the Urucum basin were derived from different provenances (Viehmann et al., 2016). If the Fe and Mn in Urucum deposits were sourced from bacterial reduction in glacial deposits, the benthic metal flux (i.e., low-temperature porewaters released from sediments on the continental slope and shelf) from sediments would have  $\epsilon\text{Nd}_t$  values of  $-8$  to  $-14$ . Such expected  $\epsilon\text{Nd}_t$  values are significantly lower than the actual

observed  $\epsilon\text{Nd}_t$  values of IF and MnF samples, which cluster around  $-4$  and  $-6$  (Viehmann et al., 2016). Therefore, the benthic flux from sediments cannot be the sole metal source for the Urucum deposits, and an additional metal source with  $\epsilon\text{Nd}_t > -4$  must have contributed to the IF and MnF at Urucum. The difference between initial  $\epsilon\text{Nd}_t$  values between clastic and chemical sediments reflect IF precipitation from water masses that tapped their rare earth element budget from chemical weathering of rocks from the nearby Brasília Belt rather than from local hinterland (Viehmann et al., 2016). Notably, no positive Eu anomalies are observed in the relatively pure precipitates of the Urucum IF-MnF (Angerer et al., 2016; Viehmann et al., 2016; Frei et al., 2017), suggesting that high-temperature hydrothermal fluids did not affect seawater chemistry in the Urucum basin (Viehmann et al., 2016). According to Cox et al. (2016), hydrothermal vents from mid-ocean ridges and potentially other young mafic rocks had an  $\epsilon\text{Nd}_t$  value of about  $+7$  during the Cryogenian. If a more felsic source was involved in producing the hydrothermal fluid (i.e., by local faulting as suggested by Freitas et al., 2011), then the  $\epsilon\text{Nd}_t$  of the hydrothermal fluid could be lower, but cannot be lower than  $-4$  at this time in the Urucum basin.

Mixing of the two sources of iron at different proportions can be modeled for Fe and Nd isotopes (Fig. 7). In the mixing model, we firstly assume that the benthic iron end member has a  $\delta^{56}\text{Fe}$  value of  $-2\text{‰}$  (a typical pore water value; e.g., Johnson et al., 2008a, 2008b) and an  $\epsilon\text{Nd}_t$  value of  $-8$  to  $-14$ , while the hydrothermal iron end member shows a  $\delta^{56}\text{Fe}$  value of  $0\text{‰}$  and an  $\epsilon\text{Nd}_t$  value of  $+7$  (Cox et al., 2016) (Fig. 7A). The Fe/Nd molar ratios for the benthic flux and hydrothermal flux are set as  $3.4 \times 10^4$  and  $1.7 \times 10^5$ , respectively, based on studies of modern marine pore fluids (Cox et al., 2016) and low-temperature hydrothermal vents (Michard et al., 1993). We use Fe/Nd molar ratio low-temperature hydrothermal vent fluid rather than high-temperature hydrothermal vent fluid as input parameter because MnF and IF samples from Urucum deposits lack positive Eu anomalies similarly to almost all reported Neoproterozoic IFs (Viehmann et al., 2015). Because oxidation and precipitation of aqueous Fe(II) induces Fe isotope fractionation, but no changes in  $\epsilon\text{Nd}_t$ , the mixing line can still be used to assess the relative contribution of Fe in the MnF and IF based on the measured  $\epsilon\text{Nd}_t$  values. As shown in Fig. 7A, Fe from benthic flux contributed 35–50% of total Fe in the MnF and IF samples to produce an  $\epsilon\text{Nd}_t$  of  $-4$  to  $-6$ , if the benthic flux had an  $\epsilon\text{Nd}_t$  value of  $-8$ . However, if the  $\epsilon\text{Nd}_t$  value of benthic flux was  $-14$  (similar to that of ambient crystalline basement), then only 18–23% of Fe in the MnF and IF samples were sourced from benthic flux.

It should be noted that the  $\epsilon\text{Nd}_t$  of hydrothermal fluids could be lower than  $+7$ , and if so, the contribution of benthic Fe to the Urucum IF and MnF should also be lower. For example, if the  $\epsilon\text{Nd}_t$  of hydrothermal fluid is set as  $0$ , then the modeling results show that the benthic flux

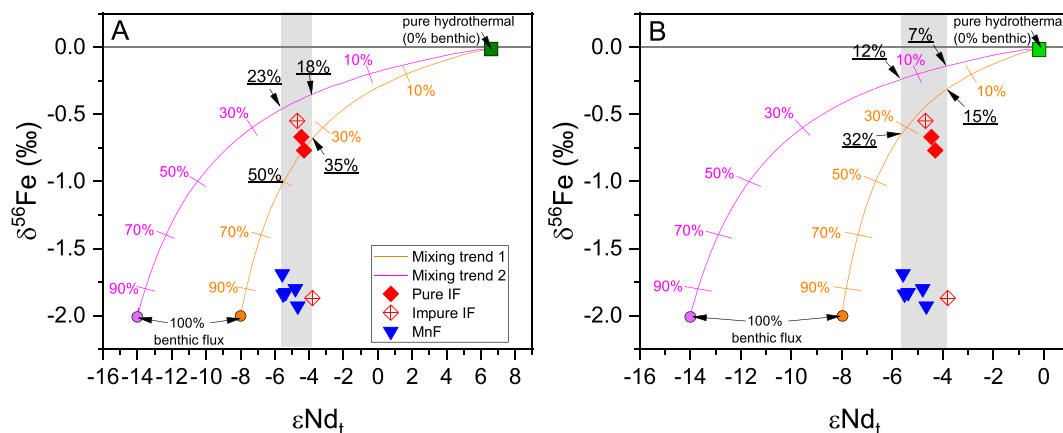


Fig. 7. Modeling results of the relation between  $\delta^{56}\text{Fe}$  and  $\epsilon\text{Nd}_t$  values for a mixture of a hydrothermal fluid (plot A:  $\epsilon\text{Nd}_t = +7$ ; plot B:  $\epsilon\text{Nd}_t = 0$ ) and a benthic flux ( $\epsilon\text{Nd}_t = -8$  or  $-14$  for both plot A and plot B) at different proportions. The percentage data next to the mixing lines denote the percentage of iron of benthic flux source in the mixture. For more details of the mixing model, see the text.

contributed 7–32% of Fe to the Urucum depositional environment (Fig. 7B). Using the mixing modeling as illustrated in Fig. 7, the  $\delta^{56}\text{Fe}$  value of the Fe source for the Urucum IF and MnF can be estimated to be around  $-1\%$  to  $-0.1\%$ , i.e., the higher the contribution from benthic Fe flux, the lower is the  $\delta^{56}\text{Fe}$  value of the Fe source. In summary, the benthic flux contributed a substantial amount (7–50%) of the metals (e.g., Fe) to the Urucum IF and MnF; however, *low-temperature* hydrothermal fluids remained to be the dominant source of metals in the Urucum IF and MnF deposits.

### 5.3. The Urucum depositional model and implications

Synthesizing the above discussions on the Fe and Nd isotope data, a depositional model for the Urucum IF-MnF is envisioned (Fig. 8). Deposition of a giant iron formation required a combination of: 1) abundant Fe and Mn sources, 2) a mechanism to effectively oxidize aqueous Fe and Mn in a relatively confined space, and 3) a stable ocean current system to deliver the aqueous Fe and Mn to the location of oxidation and precipitation. The Urucum deposits happened to meet all of these requirements. The long and narrow graben system associated with the Chiquitos–Tucavaca aulacogen hosted a vast amount of clastic sediments, which could provide benthic iron and manganese source, and faulting and volcanism related to rifting could facilitate hydrothermal activity. In addition, the upwelling current and the redoxcline could have been stable over a substantial period in an aulacogen setting, and the aulacogen could have served as a funnel of upwelling current, which provided a continuous source of metals. In a Cryogenian world, the ocean was temporarily covered by ice sheets, which cut down the interaction between oceans and the atmosphere leading to the development of anoxia in deep waters. Low-temperature fluids that were discharged from regional fault-induced hydrothermal systems were transported to the marine Urucum rift-basin associated with the Chiquitos–Tucavaca aulacogen, where thick successions of chemical sediments and glacial debris were deposited. Bacterial iron reduction took place in the sediments, supporting a steady Fe- and Mn-bearing benthic flux. The two sources of Fe were mixed by an upwelling current, which transported the Fe- and Mn-bearing fluids upwards along the shelf of the basin.

Upon deglaciation, the surface water oxygenated due to the thawing of the ice cover, and the exchange between seawater and atmosphere

sustained a redoxcline between the shallow zone of oxidizing environment and the anoxic deeper basin (Fig. 8). When the metal-bearing fluid was transported across the redoxcline, partial oxidation of aqueous Fe (II) led to the removal of isotopically heavy Fe, as well as relative enrichment of Mn(II) in the water mass. Finally, the fluid was almost depleted in aqueous Fe(II) and the oxidative potential was high enough to fully oxidize and precipitate aqueous Mn(II). Therefore, an Fe isotope gradient (decreasing  $\delta^{56}\text{Fe}$  upward and laterally) was developed across the redoxcline in a (semi-)closed basin system where Fe isotope fractionation can follow a Rayleigh fractionation process (Fig. 8). The glaciomarine environment could have fluctuated over time, and periodic retreat and advancement of the redoxcline would result in the repeated appearance of manganese ore layers as well as vertical fluctuations in  $\delta^{56}\text{Fe}$  within the Urucum iron formations.

Marine chemical sediments that contain iron oxides as the dominant Fe phases (i.e., ironstones and cherts) exhibit a large variation in Fe isotope compositions (Fig. 9). The majority of these sediments have positive  $\delta^{56}\text{Fe}$  values, which are commonly explained by partial oxidation of aqueous Fe(II) (Johnson et al., 2008a, 2008b; Beard et al., 2003; Planavsky et al., 2012). A smaller, but substantial proportion of the Fe-oxide-dominated marine chemical sediments show negative  $\delta^{56}\text{Fe}$  values that lead to different interpretations. Some researchers suggested that the low  $\delta^{56}\text{Fe}$  signatures reflected a Rayleigh process of partial aqueous Fe(II) oxidation, in which progressive removal of isotopically heavy Fe led to the depletion of  $^{56}\text{Fe}$  in aqueous solution and precipitation of low- $\delta^{56}\text{Fe}$  Fe oxides (Rouxel et al., 2005; Planavsky et al., 2012). By contrast, others argued that the low- $\delta^{56}\text{Fe}$  signatures in Fe oxides can be produced by near-quantitative oxidation of Fe(II) released by bacterial Fe reduction in sediments (Li et al., 2015; Heimann et al., 2010; Johnson et al., 2008a, 2008b; Craddock and Dauphas, 2011). Despite this dispute, this study on Urucum IF and MnF deposits shows that the low- $\delta^{56}\text{Fe}$  signatures in high-Mn iron formations or manganese formations predominantly reflect progressive oxidation of aqueous Fe (II), in agreement with previous studies on high-Mn iron formations in the Neoproterozoic and Paleoproterozoic (Tsikos et al., 2010; Kurzweil et al., 2016). In particular, the correlation between  $\delta^{56}\text{Fe}$  and Fe/Mn ratios is a clear indicator of Rayleigh type partial oxidation processes in ancient oceans, and a combination of low  $\delta^{56}\text{Fe}$  (i.e.,  $< -1.5\%$ ) and low Fe/Mn ( $< 10$ ) is a clear fingerprint for highly oxidative marine environment. Interestingly, the occurrence of such signatures coincided with

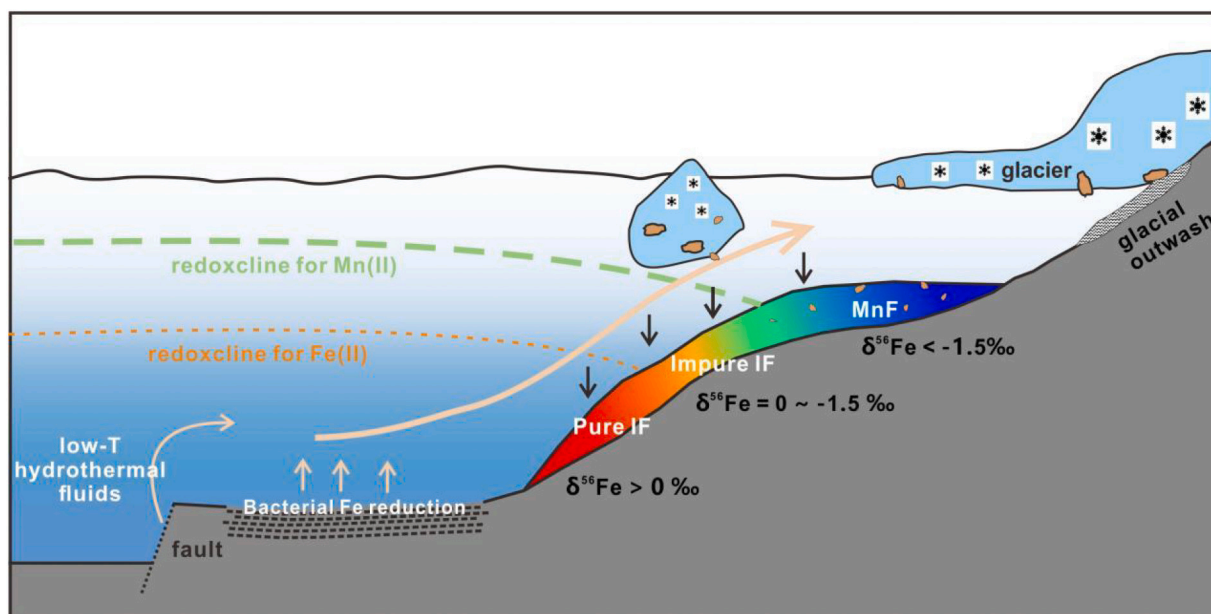
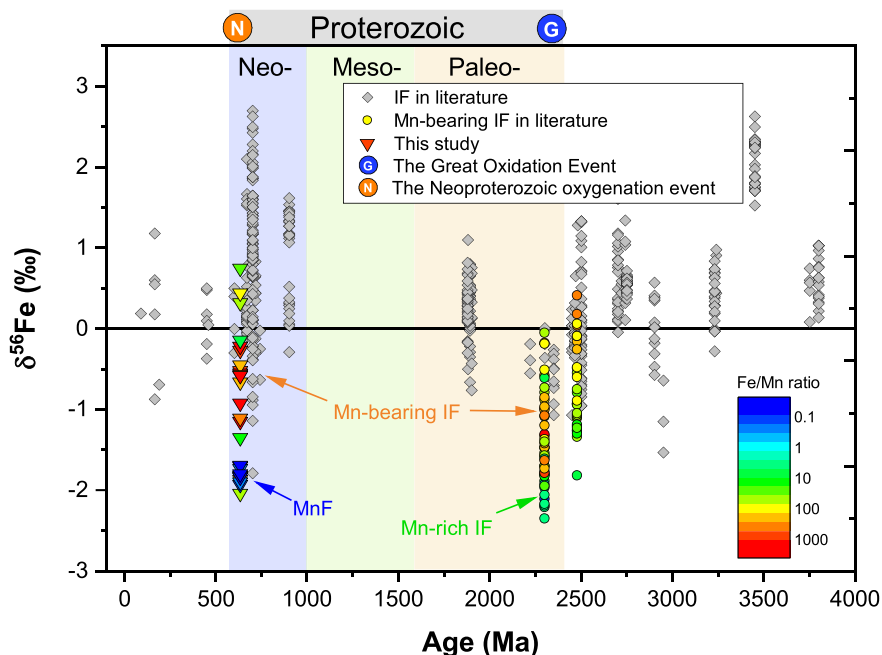


Fig. 8. A conceptual depositional model for the Urucum IF and MnF deposits.



**Fig. 9.** Compilation of  $\delta^{56}\text{Fe}$  values of Fe-oxide-bearing chemical sediments (e.g., ironstones, cherts) through time. Note that Fe isotope data of shales, carbonates and pyrite are not included in this graph. Iron isotope data for IFs are compiled from literature (e.g., McCoy et al., 2017), Fe isotope data for Paleoproterozoic and late-Archean Mn-bearing IFs are from Tsikos et al. (2010) and Kurzweil et al. (2016).

the two oxygenation events (the Great oxidation event and the Neoproterozoic oxygenation event) in Earth's history (Fig. 9).

## 6. Concluding remarks

The following conclusions can be drawn from the here presented Fe isotope study of the Late Neoproterozoic Urucum IF-MnF:

- (1) Samples of iron- and manganese- formations from the central graben system of the Cryogenian Urucum deposit show a large variation in Fe isotope composition, with  $\delta^{56}\text{Fe}$  values ranging from  $-2.04\text{‰}$  to  $0.75\text{‰}$ . The majority of the samples exhibit a positive correlation between  $\delta^{56}\text{Fe}$  values and Fe/Mn ratios, with manganese-poor ironstones generally having higher  $\delta^{56}\text{Fe}$  values and the manganese ores having lower  $\delta^{56}\text{Fe}$  values.
- (2) Both benthic flux of pore fluids and low-temperature hydrothermal fluids contributed to the seawater chemistry in the Urucum basin from which the Urucum IF-MnF deposits formed; however, over 50% of Fe was sourced from low-temperature hydrothermal systems.
- (3) The low  $\delta^{56}\text{Fe}$  values of the IF and MnF samples are primarily a result of progressive partial oxidation via Rayleigh-type fractionation of aqueous Fe(II) during its transport to the site of deposition.
- (4) Deposition of the Urucum IF and MnF can be explained by a deglaciation-oxidation model. In this model, the upwelling Fe(II)-rich bottom seawater was progressively oxidized during its transport across a redoxcline that was established after marine deglaciation. The upwelling current facilitated the oxidation of aqueous Fe(II) and Mn(II) and the deposition of ironstones and manganese oxides in the Urucum district.

## CRedit authorship contribution statement

**Qingyu Huang:** Investigation, Visualization, Writing – original draft. **Sebastian Viehmann:** Resources, Visualization, Writing – review & editing. **Detlef H.G. Walde:** Resources, Writing – review & editing.

**Weiqiang Li:** Conceptualization, Funding acquisition, Writing – original draft.

## Declaration of competing interest

The authors declare that they have no known competing financial interests or personal relationships that could have appeared to influence the work reported in this paper.

## Acknowledgements

We thank Max Lechte for help with the compilation of Fe isotope data in literature. This study is supported by the Strategic Priority Research Program (B) of the Chinese Academy of Sciences (XDB26020101) and Natural Science Foundation of China (No. 41622301) to WL. SV greatly acknowledges Bernhard Bühn and Michael Bau for organizing a field trip to the Urucum area within the joint project between the Deutsche Forschungsgesellschaft (DFG) and the Brazilian Conselho Nacional de Desenvolvimento Científico e Tecnológico (CNPq). We also greatly acknowledge the support of Adriana Zapparoli and her colleagues from the Vale Company which gave access to the mining area and the drill core samples, and a continuing helpful and pleasant cooperation.

## References

- Angerer, T., Hagemann, S.G., Walde, D.H.G., Halverson, G.P., Boyce, A.J., 2016. Multiple metal sources in the glaciomarine facies of the Neoproterozoic Jacadigo iron formation in the “Santa Cruz deposit”, Corumbá, Brazil. *Precambrian Res.* 275, 369–393. <https://doi.org/10.1016/j.precamres.2016.01.002>.
- Angerer, T., Hagemann, S.G., Walde, D.H.G., 2020. Diagenetic and supergene ore forming processes in the iron formation of the Neoproterozoic Jacadigo Group, Corumbá, Brazil. *J. S. Am. Earth Sci.*, 102902 <https://doi.org/10.1016/j.jsames.2020.102902>.
- Beard, B.L., Johnson, C.M., Skulan, J.L., Nealon, K.H., Cox, L., Sun, H., 2003. Application of Fe isotopes to tracing the geochemical and biological cycling of Fe. *Chem. Geol.* 195 (1–4), 87–117.
- Cox, G.M., Halverson, G.P., Minarik, W.G., Le Heron, D.P., Macdonald, F.A., Bellefroid, E.J., Strauss, J.V., 2013. Neoproterozoic iron formation: an evaluation of its temporal, environmental and tectonic significance. *Chem. Geol.* 362, 232–249. <https://doi.org/10.1016/j.chemgeo.2013.08.002>.

- Cox, G.M., Halverson, G.P., Poirier, A., Le Heron, D., Strauss, J.V., Stevenson, R., 2016. A model for Cryogenian iron formation. *Earth Planet. Sci. Lett.* 433, 280.
- Craddock, P.R., Dauphas, N., 2011. Iron and carbon isotope evidence for microbial iron respiration throughout the Archean. *Earth Planet. Sci. Lett.* 303 (1–2), 121–132. doi: <https://doi.org/10.1016/j.epsl.2010.12.045>.
- Dauphas, N., John, S.G., Rouxel, O., 2017. Iron isotope systematics. *Rev. Mineral. Geochem.* 82 (1), 415.
- Erwin, D.H., Laffamme, M., Tweedt, S.M., Sperling, E.A., Pisani, D., Peterson, K.J., 2011. The Cambrian conundrum: early divergence and later ecological success in the early history of animals. *Science* 334 (6059), 1091.
- Frei, R., Dössing, L.N., Gaucher, C., Boggiani, P.C., Frei, K.M., Bechárting, T., Crowe, S. A., Freitas, B.T., 2017. Extensive oxidative weathering in the aftermath of a late Neoproterozoic glaciation – evidence from trace element and chromium isotope records in the Urucum district (Jacadigo Group) and Puga iron formations (Mato Grosso do Sul, Brazil). *Gondwana Res.* 49, 1–20. <https://doi.org/10.1016/j.gr.2017.05.003>.
- Freitas, B.T., Warren, L.V., Boggiani, P.C., De Almeida, R.P., Piacentini, T., 2011. Tectono-sedimentary evolution of the Neoproterozoic BIF-bearing Jacadigo Group, SW-Brazil. *Sediment. Geol.* 238 (1), 48–70. <https://doi.org/10.1016/j.sedgeo.2011.04.001>.
- Haley, B.A., Klinkhammer, G.P., Mcmanus, J., 2004. Rare earth elements in pore waters of marine sediments. *Geochim. Cosmochim. Acta* 68 (6), 1265–1279. <https://doi.org/10.1016/j.gca.2003.09.012>.
- Heimann, A., Johnson, C.M., Beard, B.L., Valley, J.W., Roden, E.E., Spicuzza, M.J., Beukes, N.J., 2010. Fe, C, and O isotope compositions of banded iron formation carbonates demonstrate a major role for dissimilatory iron reduction in ~ 2.5 Ga marine environments. *Earth Planet. Sci. Lett.* 294 (1–2), 8–18.
- Hoffman, P.F., Macdonald, F.A., Halverson, G.P., 2011. Chapter 5 chemical sediments associated with Neoproterozoic glaciation: iron formation, cap carbonate, barite and phosphorite. *Geol. Soc. Lond. Mem.* 36 (1), 67–80. <https://doi.org/10.1144/m36.5>.
- Hoffman, P.F., Abbot, D.S., Ashkenazy, Y., Benn, D.I., Brocks, J.J., Cohen, P.A., Cox, G. M., Creveling, J.R., Donnadieu, Y., Erwin, D.H., Fairchild, I.J., Ferreira, D., Goodman, J.C., Halverson, G.P., Jansen, M.F., Le Hir, G., Love, G.D., Macdonald, F. A., Maloof, A.C., Partin, C.A., Ramstein, G., Rose, B.E.J., Rose, C.V., Sadler, P.M., Tziperman, E., Voigt, A., Warren, S.G., 2017. Snowball Earth climate dynamics and Cryogenian geology-geobiology. *Sci. Adv.* 3 (11), e1600983 <https://doi.org/10.1126/sciadv.1600983>.
- Homoky, W.B., Severmann, S., Mills, R.A., Statham, P.J., Fones, G.R., 2009. Pore-fluid Fe isotopes reflect the extent of benthic Fe redox recycling: evidence from continental shelf and deep-sea sediments. *Geology* 37 (8), 751–754. <https://doi.org/10.1130/g25731a.1>.
- Hyde, W.T., Crowley, T.J., Baum, S.K., Peltier, W.R., 2000. Neoproterozoic ‘snowball Earth’ simulations with a coupled climate/ice-sheet model. *Nature* 405 (6785), 425–429. <https://doi.org/10.1038/35013005>.
- Johnson, C.M., Beard, B.L., Klein, C., Beukes, N.J., Roden, E.E., 2008a. Iron isotopes constrain biologic and abiologic processes in banded iron formation genesis. *Geochim. Cosmochim. Acta* 72 (1), 151–169.
- Johnson, C.M., Beard, B.L., Roden, E.E., 2008b. The iron isotope fingerprints of redox and biogeochemical cycling in modern and ancient Earth. *Annu. Rev. Earth Planet. Sci.* 36 (1), 457–493.
- Kirschvink, J.L., 1992. In: Schopf, J.W., Klein, C. (Eds.), *Late Proterozoic Low-latitude Global Glaciation: The Snowball Earth*. Cambridge University Press, Cambridge, pp. 51–52.
- Klein, C., 2005. Some Precambrian banded iron-formations (BIFs) from around the world: their age, geologic setting, mineralogy, metamorphism, geochemistry, and origins. *Am. Mineral.* 90 (10), 1473–1499. <https://doi.org/10.2138/am.2005.1871>.
- Klein, C., Ladeira, E.A., 2004. Geochemistry and mineralogy of Neoproterozoic banded iron-formations and some selected, siliceous manganese formations from the Urucum District, Mato Grosso do Sul, Brazil. *Econ. Geol.* 99 (6), 1233–1244. <https://doi.org/10.2113/gsecongeo.99.6.1233>.
- Kurzweil, F., Wille, M., Gantert, N., Beukes, N.J., Schoenberg, R., 2016. Manganese oxide shuttling in pre-GOE oceans – evidence from molybdenum and iron isotopes. *Earth Planet. Sci. Lett.* 452, 69–78. <https://doi.org/10.1016/j.epsl.2016.07.013>.
- Li, Z.X., Li, X.H., Kinny, P.D., Wang, J., 1999. The breakup of Rodinia: did it start with a mantle plume beneath South China? *Earth Planet. Sci. Lett.* 173 (3), 171–181. [https://doi.org/10.1016/S0012-821X\(99\)00240-X](https://doi.org/10.1016/S0012-821X(99)00240-X).
- Li, W., Huberty, J.M., Beard, B.L., Kita, N.T., Valley, J.W., Johnson, C.M., 2013. Contrasting behavior of oxygen and iron isotopes in banded iron formations revealed by in situ isotopic analysis. *Earth Planet. Sci. Lett.* 384 (0), 132–143. <https://doi.org/10.1016/j.epsl.2013.10.014>.
- Li, W., Beard, B.L., Johnson, C.M., 2015. Biologically recycled continental iron is a major component in banded iron formations. *Proc. Natl. Acad. Sci.* 112 (27), 8193–8198. <https://doi.org/10.1073/pnas.1505515112>.
- McCoy, V.E., Asael, D., Planavsky, N., 2017. Benthic iron cycling in a high-oxygen environment: implications for interpreting the Archean sedimentary iron isotope record. *Geobiology* 15, 619–627.
- Michard, A., Michard, G., Stüben, D., Stoffers, P., Cheminée, J., Binard, N., 1993. Submarine thermal springs associated with young volcanoes: the Teahitia vents, Society Islands, Pacific Ocean. *Geochim. Cosmochim. Acta* 57 (21), 4977–4986. [https://doi.org/10.1016/S0016-7037\(05\)80003-1](https://doi.org/10.1016/S0016-7037(05)80003-1).
- Nie, N.X., Dauphas, N., Villalón, K.L., Liu, N., Heard, A.W., Morris, R.V., Mertzman, S.A., 2020. Iron isotopic and chemical tracing of basalt alteration and hematite spherule formation in Hawaii: a prospective study for Mars. *Earth Planet. Sci. Lett.* 544, 116385.
- Parry, L.A., Boggiani, P.C., Condon, D.J., Garwood, R.J., Leme, J.D.M., McIlroy, D., Brasier, M.D., Trindade, R., Campanha, G.A.C., Pacheco, M.L.A.F., Diniz, C.Q.C., Liu, A.G., 2017. Ichnological evidence for meiofaunal bilaterians from the terminal Ediacaran and earliest Cambrian of Brazil. *Nat. Ecol. Evol.* 1 (10), 1455–1464. <https://doi.org/10.1038/s41559-017-0301-9>.
- Pester, N.J., Rough, M., Ding, K., Seyfried, W.E., 2011. A new Fe/Mn geothermometer for hydrothermal systems: implications for high-salinity fluids at 13°N on the East Pacific Rise. *Geochim. Cosmochim. Acta* 75 (24), 7881–7892. <https://doi.org/10.1016/j.gca.2011.08.043>.
- Piacentini, T., Vasconcelos, P.M., Farley, K.A., 2013. 40Ar/39Ar constraints on the age and thermal history of the Urucum Neoproterozoic banded iron-formation, Brazil. *Precambrian Res.* 228, 48–62. <https://doi.org/10.1016/j.precamres.2013.01.002>.
- Planavsky, N., Rouxel, O.J., Bekker, A., Hofmann, A., Little, C.T.S., Lyons, T.W., 2012. Iron isotope composition of some Archean and Proterozoic iron formations. *Geochim. Cosmochim. Acta* 80 (0), 158–169.
- Rouxel, L.J., Bekker, N., Edwards, A.J., 2005. Iron isotope constraints on the Archean and Paleoproterozoic ocean redox state. *Science* 307, 1088–1091.
- Severmann, S., Johnson, C.M., Beard, B.L., Mcmanus, J., 2006. The effect of early diagenesis on the Fe isotope compositions of porewaters and authigenic minerals in continental margin sediments. *Geochim. Cosmochim. Acta* 70 (8), 2006–2022.
- Tsikos, H., Matthews, A., Erel, Y., Moore, J.M., 2010. Iron isotopes constrain biogeochemical redox cycling of iron and manganese in a Palaeoproterozoic stratified basin. *Earth Planet. Sci. Lett.* 298 (1–2), 125–134.
- Urban, H., Stribny, B., Lippolt, H.J., 1992. Iron and manganese deposits of the Urucum District, Mato Grosso do Sul, Brazil. *Econ. Geol.* 87 (5), 1375–1392. <https://doi.org/10.2113/gsecongeo.87.5.1375>.
- Viehmann, S., Bau, M., Hoffmann, J.E., Münker, C., 2015. Geochemistry of the Krivoy Rog Banded Iron Formation, Ukraine, and the impact of peak episodes of increased global magmatic activity on the trace element composition of Precambrian seawater. *Precambrian Res.* 270, 165–180. <https://doi.org/10.1016/j.precamres.2015.09.015>.
- Viehmann, S., Bau, M., Bühn, B., Dantas, E.L., Andrade, F.R.D., Walde, D.H.G., 2016. Geochemical characterisation of Neoproterozoic marine habitats: evidence from trace elements and Nd isotopes in the Urucum iron and manganese formations, Brazil. *Precambrian Res.* 282, 74–96. <https://doi.org/10.1016/j.precamres.2016.07.006>.
- Walde, D.H.G., Hagemann, S.G., 2007. The Neoproterozoic Urucum/Mutun Fe and Mn deposits in W-Brazil/SE-Bolivia: assessment of ore deposit models. *Z. Dtsch. Ges. Geowiss.* 158 (1), 45–55. <https://doi.org/10.1127/1860-1804/2007/0158-0045> (Tsikos et al., 2010; Kurzweil et al., 2016).
- Walde, D.H.G., Do Carmo, D.A., Guimarães, E.M., Vieira, L.C., Erdtmann, B., Sanchez, E. A.M., Adorno, R.R., Tobias, T.C., 2015. New aspects of Neoproterozoic-Cambrian transition in the Corumbá region (state of Mato Grosso do Sul, Brazil). *Ann. Paleontol.* 101 (3), 213–224. <https://doi.org/10.1016/j.annpal.2015.07.002>.
- Young, E.D., Galy, A., Nagahara, H., 2002. Kinetic and equilibrium mass-dependent isotope fractionation laws in nature and their geochemical and cosmochemical significance. *Geochim. Cosmochim. Acta* 66, 1095–1104.